JOURNAL OF MATERIALS SCIENCE 37 (2002) 753–764

Crystal plasticity analysis of earing in deep-drawn OFHC copper cups

M. GRUJICIC, S. BATCHU
Department of Mechanical Engineering, Clemson University, Clemson, SC 29634-0921, USA
E-mail: mica@ces.clemson.edu

The theory of thermally-activated slip is used to derive a crystal-plasticity materials constitutive model for deformation of OFHC copper single crystals. The mechanical response of the polycrystalline material is next determined from the single-crystalline materials constitutive relations using the classical Taylor approximation for apportionment of the deformation gradient between grains. Simulations of the deep drawing of cylindrical cups from as-rolled OFHC-copper blanks are next carried out using an explicit finite element formulation. The results obtained show that the crystallographic texture in as-rolled sheets, which can be accounted for through the use of crystal-plasticity, gives rise to rim-earing in fully-drawn cups. It is further shown that the extent of rim-earing can be greatly reduced by properly modifying the shape of the blank. A procedure is next proposed for optimization of the blank shape.

1. Introduction

Deep drawing is a process in which a flat sheet-metal blank is formed into a cylindrical or box-shaped part by means of a punch, which presses the blank into the die cavity. Despite its name, deep drawing is used for the production of not only deep but also shallow parts and the parts of moderate depth. The process was first developed in the 1700s, and has been studied extensively eversince. Currently, deep drawing represents an important metalworking process for the production of parts such as beverage cans, pots and pans, containers of all shapes and sizes, sinks and automobile panels.

In the present work, deep drawing of cylindrical cups is analyzed using finite element modeling. The basic parameters of such a process are shown in Fig. 1. A circular sheet metal blank, with the diameter D_0 and the thickness t_0, is placed over a die with the inner diameter D_d and the corner radius R_d. The blank is held in place by applying the force to a ring-shaped blankholder, with the inner diameter D_b. A punch, with the diameter D_p and the corner radius R_p, moves downward and pushes the blank into the die cavity, thus forming a cup. The major independent process variables in deep drawing are: (a) Mechanical properties of the sheet metal; (b) The ratio of the blank diameter and the punch diameter; (c) The blank thickness; (d) The clearance between the punch and the die; (e) The punch and die corner radii; (f) The blankholder force; (g) Friction and lubrication conditions at the contacting surfaces between the punch, the die, the blankholder and the blank; and (h) The speed of the punch. In the present work, the effect of sheet-metal mechanical properties and the blank shape on the shape of fully drawn OFHC copper cylindrical cups will be explored.

During a deep drawing operation, the blank is subjected to complex states of stress. A material element in the blank flange experiences a radial tensile stress because the blank is being pulled into the die cavity. In addition a compressive stress acts in the through thickness direction as a result of a force applied to the blankholder. Also a compressive hoop stress develops in the element as the blank circumference is being reduced during drawing. These hoop stresses tend to cause the flange to wrinkle during drawing, thus requiring the use of a blankholder and the adequate holding force. Under this state of stress, an element in the flange contracts in the hoop direction and elongates in the radial direction. A material element in the cup wall is subjected to a longitudinal tensile stress, as the force applied to the punch is transmitted through the walls of the cup to the flange that is being drawn into the die cavity. In addition, a tensile hoop stress develops since the rigid punch prevents radial contraction of the cup as the latter is being drawn. Consequently, an element in the cup wall elongates in the longitudinal (axial) direction without undergoing a change in its width.

An important aspect of deep drawing is the relative contributions of stretching and pure drawing. When the blankholder force is too high, the blank is prevented from flowing freely into the die cavity. The deformation of the sheet metal takes place mainly under the punch and the sheet begins to stretch, eventually resulting in necking and tearing. Conversely, a small blankholder force allows the blank to flow freely into the die cavity (pure drawing). In this case, the plastic deformation takes place mainly in the flange, while the cup wall is subjected only to elastic stresses. However, these stresses increase with increasing the D_0/D_p ratio and

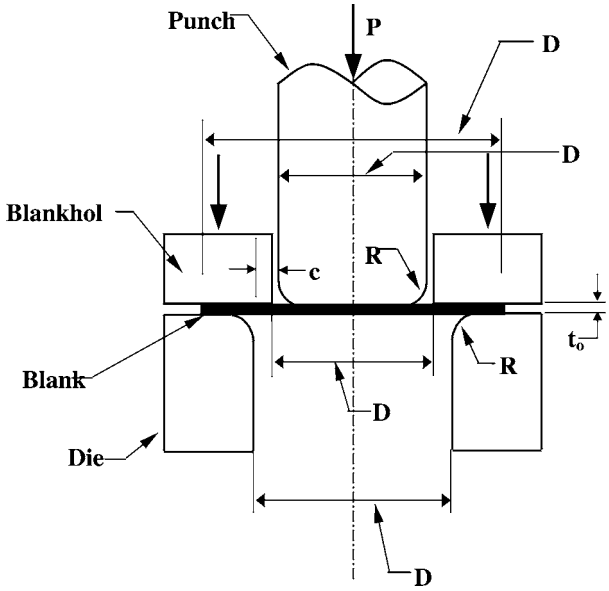

Figure 1 Variables in deep drawing of a cylindrical cup. Except for the punch force, all process variables are independent variables. See Table II and text for identity of the variables.

can lead to failure when the cup wall cannot support the load required to draw in the flange.

In addition to flange wrinkling and wall tearing discussed above, development of ears along the rim of fully-drawn cups is another important aspect of deep drawing. Rim ears (referred to as earing in the following) are generally caused by anisotropic properties of the sheet-metal blank material. These ears must be trimmed off to produce the desired height and shape of fully drawn cups which introduces an additional processing step (trimming) and, thus, increases the manufacturing cost. Hence, a better understanding of the process of development of cup ears during deep drawing could lead to improved process designs which can reduce formation or even eliminate earing and thus the need for trimming.

The quantitative prediction of earing patterns has been attempted with moderate success by many researchers (e.g., Tucker [1], Wilson and Butler [2], Becker *et al*. [3]). The major limitation in all these attempts was an inability to simulate the deep drawing process until a fully drawn cup is obtained. Recently, however, Anand and Balasubramanian [4] developed a crystal-plasticity materials constitutive model for polycrystalline Al2008-T4 alloys and introduced a finite element procedure to simulate the formation of ears in fully drawn cups. In the present work, the analysis carried out by Anand and Balasubramanian [4] is extended to OFHC copper and also includes optimization of the shape of the sheet-metal blank in order to minimize the extent of earing in a fully drawn cup.

The organization of the paper is as following: A brief description of the materials constitutive relations for single and polycrystalline OFHC copper and the integration of the material state is discussed in Section 2. A procedure for assigning the initial crystallographic texture to the blank material, finite element modeling of deep drawing of a cylindrical cup and a brief overview of the Simplex optimization method used to determine the optimum blank shape are all presented in Section 3. The main findings obtained in the present work are presented and discussed in Section 4. In Section 5, a summary is given of the main conclusions resulted from the present work.

2. Materials constitutive model

The deformation behavior of the blank material is described using a finite-deformation, rate- and temperature-dependent crystal-plasticity constitutive model for single crystalline metallic materials with the face-centered-cubic (f.c.c.) crystal structure recently proposed by Balasubramanian [4]. Within this model, the shearing rates on slip systems are represented using a physically-motivated constitutive function based on the theory of thermally-activated plastic flow. To account for the polycrystalline character of the blank materials, the classical Taylor approximation, which postulates a uniform partitioning of the deformation gradient among the grains, is invoked. The constitutive model is implemented in the commercial finite-element package ABAQUS/Explicit. The material parameters for OFHC copper derived by Grujicic [5] are used in the simulations.

2.1. Single crystal constitutive model

The continuum mechanics foundation for the crystal plasticity constitutive model used in the present work can be traced to the work of Teodosiu [6], Hill and Rice [7], Mandel [8], Teodosiu and Sidoroff [9], Asaro and Rice [10] and Asaro [11]. The work of Conrad [12], Kocks *et al*. [13], Frost and Ashby [14], and Argon [15], on the other hand, provides a more materials science viewpoint of the subject matter.

The deformation of a single crystal is considered to be the result of two independent atomic-scale processes: (i) an elastic distortion of the crystal lattice corresponding to the stretching of atomic bonds and; (ii) a plastic deformation which is associated with atomic plane slippage which leaves the crystal lattice undisturbed. At lower temperatures ($T < 0.3T_m$, $T_m =$ melting temperature) and at sufficiently high stress levels, the major mechanism of plastic deformation in ductile single-crystalline metallic materials is dislocation glide on well-defined crystallographic slip planes. While other plastic deformation mechanisms such as twinning, martensitic transformation, etc., can also take place in some metallic materials, crystallographic slip (referred to as slip in the following) is the only plastic deformation mechanism considered in the present work.

The constitutive model used in the present work is based on the following governing variables: (i) The Cauchy stress, T, a second-order tensor; (ii) The deformation gradient, F a second-order tensor; (iii) The absolute temperature θ, (iv) Crystal slip systems, labeled by integers α. Each slip system is specified by a unit normal n_0^α to the slip plane, and a unit vector m_0^α aligned in the slip direction in the initial (reference) configuration. In f.c.c. metallic materials, such as OFHC copper, there are 12 slip systems and they are all based on $\{111\}$ crystallographic planes and $\langle 1\bar{1}0\rangle$ crystallographic directions. The orientation of the slip systems (m_0^α, n_0^α)

in each grain relative to the global coordinate system is readily determined from the known crystallographic orientation of the grain; (iv) The plastic deformation gradient, F^p, a second-order tensor, with $\det F^p = 1$ since plastic deformation by slip does not give rise to a volume change and; (v) The slip system deformation resistance $s^\alpha > 0$ which has the units of stress.

The deformation gradient can be multiplicatively decomposed as $F = F^e F^p$ where the elastic deformation gradient F^e is defined by:

$$F^e \equiv F F^{p-1}, \quad \det F^e > 0. \tag{1}$$

and describes the elastic distortions and rigid-body rotations of the crystal lattice. The plastic deformation gradient, F^p, on the other hand, accounts for the cumulative effect of shearing on the active slip systems in the crystal.

2.1.1. Constitutive equation for stress

Since elastic stretches in metallic materials are generally small and the temperature changes accompanying deep drawing are not expected to be significant, the constitutive equation for stress in a metallic single crystal can be defined by the linear relation:

$$T^* = C[E^e - A(\theta - \theta_0)] \tag{2}$$

where C is a fourth-order anisotropic elasticity tensor, and A, a second-order anisotropic thermal expansion tensor and θ_0 a reference temperature. E^e and T^* are respectively the Green elastic strain measure and the second Piola-Kirchhoff stress measure relative to the configuration obtained after plastic shearing of the lattice as described by F^p. E^e and T^* are respectively defined as:

$$E^e \equiv (1/2)\{F^{eT} F^e - I\} \quad T^* \equiv (\det F^e) F^{e-1} T F^{e-T} \tag{3}$$

where I is the second order identity tensor.

2.1.2. Flow rule

The evolution of the plastic deformation gradient, F^p, is defined by the following rate equations:

$$\dot{F}^p F^{p-1} = \sum_\alpha \dot{\gamma}^\alpha S_0^\alpha \quad S_0^\alpha \equiv m_0^\alpha \otimes n_0^\alpha \tag{4}$$

where S_0^α is generally referred to as the Schmid tensor, $\otimes$ designates the tensorial product, subscript 0 indicates that the quantity in question is expressed relative to the initial configuration, and:

$$\dot{\gamma}^\alpha = \rho_m^\alpha b \bar{v}^\alpha \tag{5}$$

is the plastic shearing rate on slip system α. The expression $\dot{\gamma} = \rho_m b \bar{v}$ was originally introduced by Orowan [16] to represent the physical picture that plastic shearing is the result of motion of a density ρ_m of mobile dislocations, each with the Burgers vector of magnitude b and aligned in the slip direction m_0, and moving at an average velocity $\bar{v}$.

In metallic materials where the elastic stretches are generally small, the resolved shear stress τ^α, on slip system α, which gives rise to the motion of the dislocations associated with that slip system is defined as:

$$\tau^\alpha \equiv T^* \cdot S_0^\alpha \tag{6}$$

where the raised dot indicates the scalar product of two second order tensors.

To derive an expression for the average dislocation velocity, the theory of thermally activated dislocation motion is invoked. According to this theory, at a finite temperature, the local resistance to dislocation motion due to short-range obstacles (obstacles smaller than ~10 atoms in diameter) can be overcome at a lower applied shear stress with the help of redistribution of the thermal energy (referred to as thermal activation in the following). Consequently, the dislocations associated with a slip system can acquire a finite velocity at shear stress levels below the slip resistance s^α associated with that slip system.

The resistance to slip arises from various obstacles which impede dislocation motion. In general, one distinguishes between the *thermal* obstacles that can be overcome with the aid of thermal activation, and the *athermal* obstacles which are too broad or too strong (or both) and thus cannot be thermally overcome. Consequently, the slip resistance s^α is decomposed as:

$$s^\alpha = s_*^\alpha(\theta, \mathit{microstructure}) + s_a^\alpha(\theta, \mathit{microstructure}) \tag{7}$$

where s_*^α represents the part of the slip resistance associated with the thermally-activatable obstacles (referred to as thermal obstacles in the following), and s_a^α is the part of the slip resistance arising from thermally-nonactivable obstacles (referred to as athermal obstacles in the following), which are either too strong or too long-range (or both) to be overcome by the aid of thermal activation. Typical examples of thermal obstacles are the Peierls resistance, solute atoms, and forest dislocations whereas dislocation groups and large incoherent precipitates typify athermal obstacles. In pure f.c.c. materials, such as OFHC copper, the Peierls resistance to dislocation motion is quite small and s_*^α is dominated by interactions between the mobile dislocations and the localized forest dislocations. For the further analysis, it is convenient to introduce an effective shear stress as:

$$\tau_*^\alpha \equiv |\tau^\alpha| - s_a^\alpha \tag{8}$$

then, according to the theory of thermally-activated dislocation motion, the shearing rate on slip system α may be expressed as:

$$\dot{\gamma}^\alpha = \begin{cases} 0 & \text{if } \tau_*^\alpha \le 0, \\ \dot{\gamma}_0^\alpha v \exp\left\{-\dfrac{\Delta G_*^\alpha(\tau_*^\alpha, s_*^\alpha)}{k_B \theta}\right\} \operatorname{sign}(\tau^\alpha) & \text{if } 0 < \tau_*^\alpha < s_*^\alpha \end{cases} \tag{9}$$

where $\gamma_0^\alpha = \rho_m^\alpha b \bar{l}^\alpha v$, $\bar{l}^\alpha$, denotes the mean distance of advance of a mobile dislocation between two consecutive obstacles, v is a frequency of dislocation vibration (of the order of 10^{12} sec^{-1} i.e. 10^{-2}–10^{-1} times the Debye frequency of atoms). The quantity $[\exp\{-\frac{\Delta G_*^\alpha}{k_B\theta}\}]$ in Equation 9 represents the probability that the energy ΔG_*^α (or larger), which is required for the dislocations to overcome a thermal obstacle will be supplied through redistribution of the thermal energy at a temperature θ. ΔG_*^α is generally referred to as the Gibbs free activation energy, and k_B is the Boltzmann's constant. The rate at which dislocations overcome the thermal obstacles in question is given by $v[\exp\{-\frac{\Delta G_*^\alpha}{k_B\theta}\}]$. For simplicity, the pre-exponential term $\dot{\gamma}_0^\alpha$ in Equation (g) is taken to be the same for all slip systems, denoted by $\dot{\gamma}_0$, and assigned a value in the typical range between 10^6 and 10^7 sec^{-1}. Furthermore, while the mobile dislocation density, ρ_m^α, which contributes to $\dot{\gamma}_0$, is generally a function of the applied stress and the temperature [13], such dependencies are neglected in the present work.

Following Kocks *et al.* [13], the Gibbs free activation energy function is expressed as:

$$\Delta G_*^\alpha = \Delta F_* \left[1 - \left(\frac{\tau_*^\alpha}{s_*^\alpha} \right)^p \right]^q \tag{10}$$

where ΔF_* is the Gibbs free activation energy required to overcome an obstacle to slip without the aid of an applied shear stress. ΔF_* is generally assumed to be the same for all slip systems and to remain constant, provided the character of the obstacles does not change during slip. Parameters p and q typically fall in the ranges $0 \le p \le 1$, and $1 \le q \le 2$ and they control the shape of the ΔG_*^α versus $(\frac{\tau_*^\alpha}{s_*^\alpha})$ curve.

2.1.3. Evolution equations for slip system resistances

As plastic deformation proceeds, metallic materials become increasingly more difficult to deform. To account for such "strain-hardening", evolution of the slip system resistance parameters s^α during plastic deformation is represented by the following rate equation:

$$\dot{s}^\alpha = \sum_\beta h^{h\beta} |\dot{\gamma}^\beta|, \tag{11}$$

where $\dot{\gamma}^\beta$ is the shearing rate on slip system β, and the matrix $h^{\alpha\beta}$ describes the rate of increase of the slip resistance on slip system α due to shearing on both coplanar (self hardening) and non-coplanar (latent hardening) slip systems β. Each element of the matrix $h^{\alpha\beta}$ evolves during deformation of the given material point. The use of the absolute value of $\dot{\gamma}^\beta$ in Equation 11 reflects the fact that the hardening behavior is assumed not to be significantly affected by the direction of shearing on a slip system.

Since the slip resistance s^α is decomposed as $s^\alpha = s_*^\alpha + s_a^\alpha$, Equation 7, it is important to determine whether the macroscopic strain hardening arises due to the changes in s_*^α, or s_a^α, or both. In pure f.c.c. materials, where s_*^α and s_a^α are both controlled by the interactions of mobile and forest dislocations [17], they evolve with strain and contribute to macroscopic strain hardening. By performing a series of temperature-jump tension-test experiments on aluminum single crystals oriented for single slip, Cottrell and Stokes [18] showed that the ratio of the thermal to the athermal deformation resistance:

$$\chi = \frac{s_*^\alpha}{s_a^\alpha}, \quad 0.5 \le \chi \le 1 \tag{12}$$

is essentially constant during plastic deformation. Since both aluminum and OFHC copper have an f.c.c. crystal structure, χ is assumed to remain constant and that it is the same for all slip systems.

Using the Equation 12, the evolution equation for s^α for f.c.c. single-crystal metallic materials can be written as:

$$\dot{s}^\alpha = \dot{s}_a^\alpha + \dot{s}_*^\alpha \doteq \dot{s}_a^\alpha \{1 + \chi\} = \sum_\beta h^{\alpha\beta} |\dot{\gamma}^\beta| \tag{13}$$

While the hardening matrix $h^{\alpha\beta}$ is the topic of active current research, several simple phenomenological forms for it have been proposed in the past. These have been reviewed by Peirce *et al.* [19], Asaro and Needleman [20], and more recently by Havner [21], and Bassani [22]. In the present work, the following $h^{\alpha\beta}$ function initially proposed by Peirce *et al.* [19] and Asaro and Needleman [20] is used:

$$h^{\alpha\beta} = \left[q_l + (1 - q_l)\delta^{\alpha\beta} \right] h^\beta \tag{14}$$

where h^β denotes the self-hardening rate and the parameter q_l represents the ratio of the latent and the self-hardening rates. While both h^β and q_l may evolve with deformation, q_l is frequently set to a fixed value (typically 1.4). This simplification is adopted in the present work. Following Kalidindi *et al.* [23], the self-hardening rate is assigned the following functional form:

$$h^\beta = h_0^\beta \left| 1 - \frac{s^\beta}{s_s^\beta} \right|^r \operatorname{sign}\left(1 - \frac{s^\beta}{s_s^\beta} \right), \tag{15}$$

where:

$$h_0^\beta = \hat{h}_0^\beta (|\dot{\gamma}^\beta|, \theta) \tag{16}$$

is the initial hardening rate, and:

$$s_s^\beta = \hat{h}_s^\beta (|\dot{\gamma}^\beta|, \theta) \tag{17}$$

is a saturation value of s^β. As implied in Equations 16 and 17, both h_0^β and s_s^β are in general expected to depend on strain rate and temperature. For simplicity, however, they are considered to be constant in the present work. It should be further noted that Equation 15 does not capture some of the details of the hardening phenomena in single-crystalline f.c.c. materials such as stage I strain hardening (easy glide), stage II strain hardening

(linear hardening), etc. This should not be considered as a significant limitation of the present model, since the single-crystalline constitutive model presented here is used only to predict the polycrystalline material behavior which does not display distinct stages of strain hardening.

2.2. Polycrystalline material constitutive model

The materials constitutive relations derived in the previous section pertain to single-crystalline materials. The sheet-metal blank, on the other hand, is generally composed of a polycrystalline material. To derive the polycrystalline material response from the single crystalline constitutive relations, the classic Taylor approximation [24, 25] is adopted. According to this approximation, the local deformation gradient in each grain is assumed to be homogeneous and identical to the macroscopic deformation gradient. This in turn yields a constant Cauchy stress within each grain. If the Cauchy stress in grain k is denoted by $T^{(k)}$, and if a continuum material point is assumed to be composed of N grains, then the volume-averaged Cauchy stress is simply given as:

$$\bar{T} = \sum_{k=1}^{N} \upsilon^{(k)} T^{(k)} \tag{18}$$

where $\upsilon^{(k)}$ is the volume fraction of grain k. If it is further assumed that all grains have equal volume, the average Cauchy stress $\bar{T}$ becomes the number average over all the grains, i.e.:

$$\bar{T} = \frac{1}{N} \sum_{k=1}^{N} T^{(k)} \tag{19}$$

While it is apparent that the Taylor approximation does not ensure the equilibrium between the adjacent grains, recent work of Bronkhorst *et al.* [26] and Kothari and Anand [27] showed that this approximation can reasonably well account for the experimentally observed texture evolution and the macroscopic stress-strain response in both f.c.c. and b.c.c. metallic materials.

2.3. Numerical integration of the material state

The polycrystalline material constitutive model discussed in the previous section is implemented in a User Material Subroutine (VUMAT) of the commercial finite element program ABAQUS/Explicit [28], which enables "dynamic, explicit" analysis of boundary value problems and is particularly suitable for the problems involving surface contacts as is the present case. At the beginning of each time increment, (time $= t$), for each element and each integration point, ABAQUS/Explicit calls the VUMAT subroutine and provides it with the following information:

TABLE I Properties of OFHC copper used in the present work

Property	Symbol	Value	Units	Equation where used
Elastic constant	C_{11}	170	GPa	[2]
Elastic constant	C_{12}	124	GPa	[2]
Elastic constant	C_{44}	75	GPa	[2]
Thermal slip resistance	s^*	672	MPa	[8]
Athermal slip resistance	s_a	30	MPa	[8]
Reference shearing rate	$\dot{\gamma}_0$	1.52×10^7	s^{-1}	[9]
Activation energy	ΔF_*	2.85×10^{-19}	J	[10]
Exponent	p	0.26	N/A	[10]
Exponent	q	1.40	N/A	[10]
Latent hardening parameter	q_1	1.4	N/A	[14]
Self-hardening parameter	h_o	180	MPa	[15]
Saturation value of slip resistance	s_s	148	MPa	[15]
Self-hardening exponent	r	2.25	N/A	[15]
Initial slip resistance	s_0	16	MPa	[11]

(i) A list of materials parameters listed in Table I;
(ii) The time-independent slip system parameters (m_0^α, n_0^α) for each grain k. It should be noted that in order to simplify notation, the grain-denoting index k is not used in the rest of this section;
(iii) A list of variables: $\{F(t), F^P(t), s^\alpha(t), \bar{T}(t)\}$; and
(iv) A kinematic estimate of the deformation gradient $F(\tau)$ at the end of the time increment (time $= \tau$).

Within the VUMAT, a conditionally-stable, accurate and efficient computational procedure is used to determine the variables $F^p(\tau)$, $s^\alpha(\tau)$, *and* $T(\tau)$ at the end of the time increment. In the present work, an Euler forward integration scheme is developed to determine evolution of the material state during loading. The procedure involves the following major steps:

(1) An inverse of the plastic deformation gradient, $F^{p^{-1}}(\tau)$, is first computed as:

$$F^e(t) = F(t) F^{p^{-1}}(t) \tag{20}$$

$$E^e(t) = \frac{1}{2}\{F^e(t)^T F^e(t) - I\} \tag{21}$$

$$T^*(t) = C(E^*(t)) \tag{22}$$

$$\tau^\alpha(t) = T^*(t) \cdot S_0^\alpha \tag{23}$$

$$\Delta\gamma^\alpha(t) = \begin{cases} 0 & \text{if} \quad \tau_*^\alpha(t) < 0 \\ \dot{\gamma}_0^\alpha \Delta t v \exp\left\{-\dfrac{\Delta G_*^\alpha(\tau_*^\alpha(t), s_*^\alpha(t))}{k_B\theta}\right\} \operatorname{sign}\{\tau^\alpha(t)\} & \text{if} \quad 0 < \tau_*^\alpha(t) < s_{*(t)}^\alpha \end{cases} \tag{24}$$

$$F^{p^{-1}}(\tau) = F^{p^{-1}}(t)\left\{I - \sum_{\alpha} \Delta\gamma^{\alpha}(t) S_0^{\alpha}\right\} \quad (25)$$

(2) Next, the Cauchy stress T (τ) in each grain at the end of the time increment is computed as:

$$F^{e}(\tau) = F(\tau)F^{p^{-1}}(\tau) \quad (26)$$

$$E^{e}(\tau) = \frac{1}{2}\{F^{e}(\tau)^{T} F^{e}(\tau) - I\} \quad (27)$$

$$T^{*}(\tau) = C(E^{*}(\tau)) \quad (28)$$

$$T(\tau) = \det(F^{*}(\tau))^{-1} F^{*}(\tau) T^{*}(\tau) F^{*}(\tau)^{T} \quad (29)$$

(3) The slip resistances $s^{\alpha}(\tau)$ are next updated as:

$$h^{\alpha\beta}(t) = q^{\alpha\beta}\left|1 - \frac{s^{\beta}(t)}{s_s}\right|^{r} \operatorname{sign}\left\{1 - \frac{s^{\beta}(t)}{s_s}\right\} \quad (30)$$

$$s^{\alpha}(\tau) = s^{\alpha}(t) + \sum_{\beta} h^{\alpha\beta}(t)|\Delta\gamma^{\beta}(t)| \quad (31)$$

(4) Finally the volume averaged Cauchy stress is computed as:

$$\bar{T}(\tau) = \frac{1}{N}\sum^{N} T(\tau) \quad (32)$$

and a list of variables: $\{F^{p}(\tau), s^{\alpha}(\tau), \bar{T}(\tau)\}$ is passed back to ABAQUS.

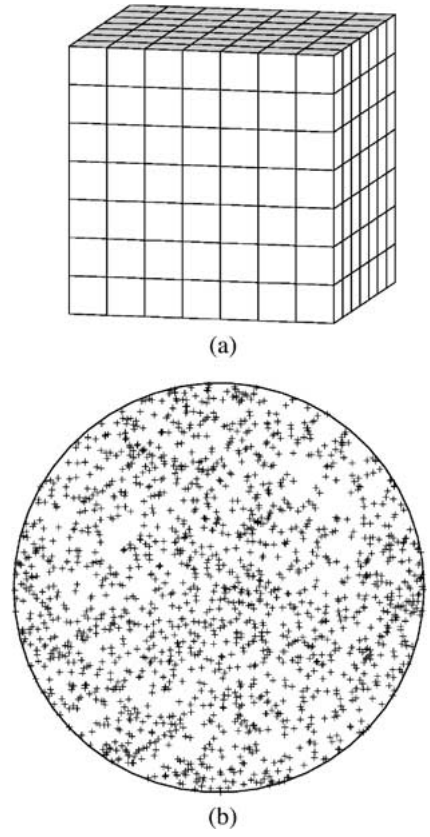

Figure 2 (a) A 343-element mesh used in the finite element simulation of flat rolling; (b) (111) equal-area projection pole figure showing a random crystallographic orientation of the 343 grains.

3. Computational procedure

3.1. Simulation of flat rolling

Since the blanks are generally obtained by stamping as-cold rolled sheet metal, they inherit the morphological and the crystallographic texture of the sheet metal. Flat rolling is generally considered as a plane-strain deformation process in which the material is elongated in the rolling direction (RD) and reduced in thickness but does not undergo significant plastic deformation in the transverse direction (TD). To assign initial crystallographic texture to the blank, flat rolling is first simulated as a plane-strain compression process using ABAQUS/Explicit. A cubic slab containing 343 cubic, continuum, three-dimensional eight-noded, reduced-integration elements (C3D8R-ABAQUS designation), Fig. 2a, is used to represent a polycrystalline slab of OFHC copper in the as-annealed condition. Each element is assumed to represent a grain and each grain is assigned a different initial crystallographic orientation by sampling the Euler angles from the random distribution. A (111) equal-area projection pole figure showing the random orientation of grains in the initial configuration is shown in Fig. 2b. (100) and (110) pole figures for the 343-grain slab (not shown here for brevity) further confirm that the initial orientation of the grains is random. 343 elements were chosen as a trade-off between the requirement for a large number of grains to represent a polycrystalline material and the desire to limit the computation time. Also, a sufficiently high value of the hourglass stiffness is used in conjunction with the reduced integration elements to suppress locking of the nodes.

The deformed mesh for the 343-grain slab after a logarithmic strain of -1.2 (a typical strain level in as cold-rolled ductile sheet metal) is applied in the through-the-thickness direction is shown in Fig. 3a. The (100), (110) and (111) equal area projection pole figures in the "as-rolled" slab are shown in Fig. 3b–d respectively. The pole figures are fully consistent with their experimental counterparts [26]. In particular, the (111) pole figure shows a diffuse dumbbell-like shape, which is the key feature of the experimentally measured (111) equal-area projection pole figure [26].

3.2. Simulation of deep drawing

Fig. 4 shows the finite-element meshes for the blank, the punch, the die, and the blankholder used in finite element modeling of the deep drawing process. To represent the blank, a total of 16 C3D6 and 320 C3D8R ABAQUS elements are used, with 1 element through the blank thickness. Each element is taken to contain 343 grains and to initially have the as cold-rolled texture shown in Fig. 3b–d. Since the initial texture of the sheet possess an orthotropic symmetry, only a 90° sector of the circular blank is analyzed. The die, blankholder and punch are all treated as rigid surfaces. The friction coefficient for the contacting surface between the punch and the blank top is set to a typical value of $\mu = 0.1$ and all other contacting surfaces are considered frictionless. The values of the main geometrical parameters for the

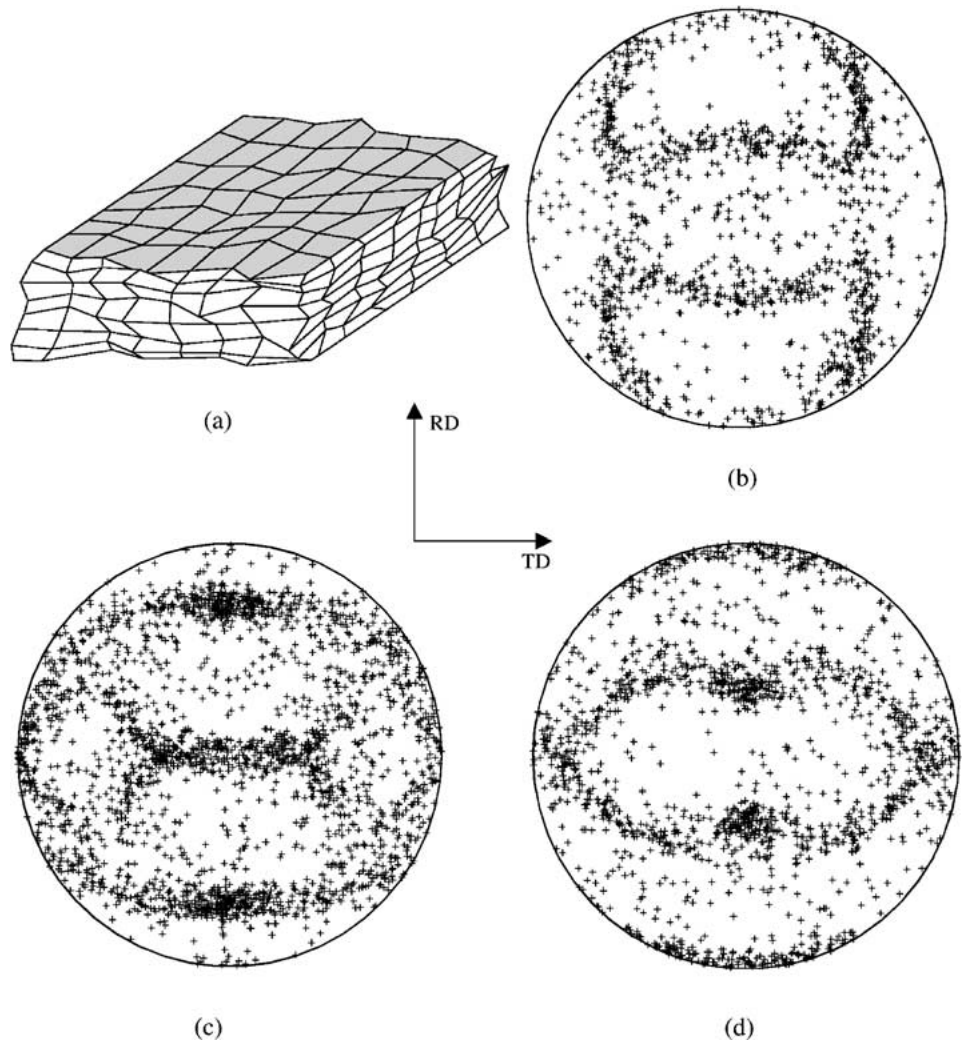

Figure 3 (a) The 343-element mesh after plane-strain compression in the through- the-thickness direction by a true strain of −1.2. (b), (c) and (d) the corresponding (200), (220) and (111) equal-area projection pole figures, respectively. The Rolling (RD) and the zero-strain transverse (TD) directions relative to the pole figures are indicated.

TABLE II Sheet-metal blank and tools geometric parameters used in the FEM simulation of deep drawing a cup. All parameters are in mm

Parameter	Symbol	Value
Blank diameter	D_0	101.6
Blank thickness	t_0	0.889
Punch diameter	D_p	50.8
Punch corner radius	R_p	5.08
Die inner diameter	D_d	53.0352
Die corner radius	R_d	5.08
Blankholder inner diameter	D_b	58.42

blank, the die, the blankholder, and the punch used in the present work are given in Table II. A moderate clamping force was chosen to avoid flange wrinkling when the clamping force is too low and cup-wall stretching when this force is too high.

Deep drawing is generally considered as an essentially quasi-static process. Such processes are typically modeled using a static, implicit finite element procedure. However, Nagtegaal and Taylor [29] demonstrated that the dynamic, explicit finite element procedure, of the type implemented in ABAQUS/Explicit, in which the solution of individual time increments is inexpensive, is generally computationally more efficient for large three-dimensional problems which are dominated by contact, such as the problem at hand.

Within ABAQUS/Explicit, a central-difference integration rule is used in the dynamic, explicit procedure to solve for velocities and accelerations from the momentum balance equations. This integration procedure is only conditionally stable, and the stable time increment is given as:

$$\Delta t_{cr} = \min\left(\frac{L^e}{c_d}\right), \tag{33}$$

where L^e is the characteristic element length, and c_d is the dilatational elastic wave speed in the material. For a cubic material, such as OFHC copper, $c_d = [(C_{12} + 2C_{44})/\rho]^{1/2}$, where C_{12} and C_{44} (as well as C_{11}) are the cubic elastic constants and ρ is the blank material density. For the Euler-forward computational procedure discussed in Section 2.3, to be stable, the strain increment within a time increment Δt is limited by the condition [30]:

$$\Delta\varepsilon = \dot{\varepsilon}\Delta t \leq 0.5\, m\, \varepsilon_y, \tag{34}$$

where m is the rate-sensitivity parameter and ε_y is the strain at the stress level equal to the yield stress.

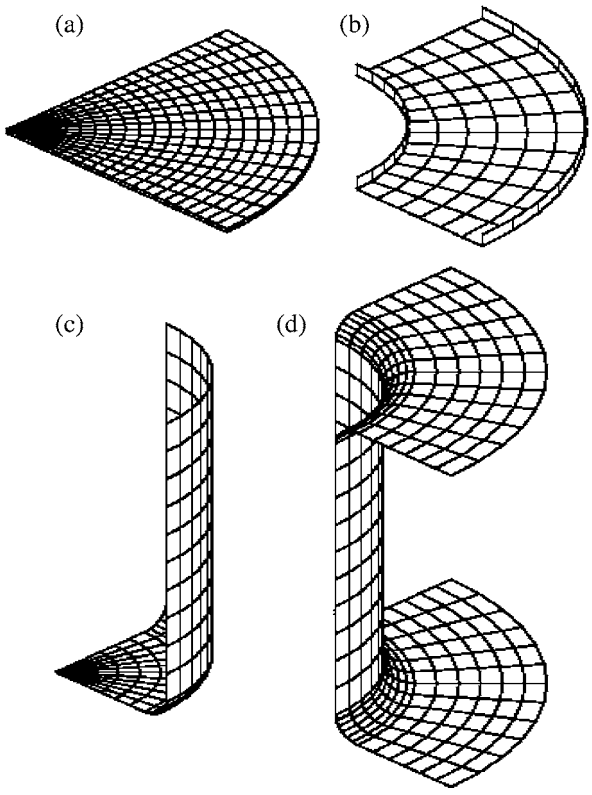

Figure 4 Finite element meshes for: (a) the blank; (b) the blankholder; (c) the punch and (d) the die used in the finite element modeling of deep drawing.

Combination of Equations 33 and 34 yields:

$$\dot{\varepsilon} \leq 0.5m\varepsilon_y \max\left(\frac{c_d}{L^e}\right) \tag{35}$$

For typical values, $m = 0.02$, $\varepsilon_y = 0.001$, $c_d = 5000m$ sec^{-1} and $L^e = 10^{-4}m$, Equation 35 yields $\dot{\varepsilon} \leq 500$ sec^{-1}. Hence, the material integration procedure presented in Section 2.3 should not be used at strain rates higher than 500 sec^{-1}.

The materials constitutive model developed in the present work is limited to the isothermal and adiabatic conditions. For the isothermal case, θ is set to θ_0 and the second term on the right hand side of Equation 2 becomes identically zero. For the adiabatic case, the temperature is determined by integration of the following equation:

$$\rho c\dot{\theta} = \xi \sum_{k=1}^{N} \left(\sum_{a} \tau^{\alpha}\dot{\gamma}^{\alpha} \right)^{(k)} \tag{36}$$

where, the first sum is over all slip systems α in a grain, and the second sum is over all grains k in a polycrystalline aggregate comprising a material point, c is the specific heat, and $0.85 \leq \xi \leq 1$ represents the fraction of plastic work converted to heat. Only the isothermal case is considered in the present work.

In order to speed-up the simulation, the stable time increment is artificially increased by increasing the density of the blank material. To ensure that in such "density-scaled" simulations the inertial effects remain small, the ratio of the total kinetic energy to the sum of stored elastic and dissipated plastic energies is monitored, and the density adjusted to prevent this ratio from exceeding 0.01 at any time during the simulation.

3.3. Optimization of the blank shape

The shape of the blank in the first quadrant of the x-y plane (the plane of the blank) is described as:

$$x^a + \frac{y^a}{b^a} = R_0^a \tag{37}$$

where a and b are design parameters which are determined using an optimization algorithm. When $a = 2$ and $b = 1$, the blank assumes the familiar circular-disk shape with a radius of R_0, Fig. 5. Optimization of the blank shape is carried out under a constant value of $R_0 = 50.8$ mm. When $a = 2$ and $b \neq 1$, the blank adopts an ellipsoidal-disk shape and b denotes the ratio of the y-based major axis and the x-based major axis of the ellipse. Two additional blank shapes corresponding to characteristic values of a and b are depicted in Fig. 5.

To optimize the blank shape for reduction/elimination of the cup earing the following objective function, which should be minimized, is defined in the present work:

$$G = \sum_{i=1}^{M} (z_i - z_{min}) \tag{38}$$

where M is the total number of nodes along the cup rim and z_i and z_{min} respectively represent the z-coordinate of a cup-rim node i and the cup-rim node with the smallest z- coordinate. In the absence of earing, $z_i = z_{min} (i = 1, M)$ and, hence, $G = 0$.

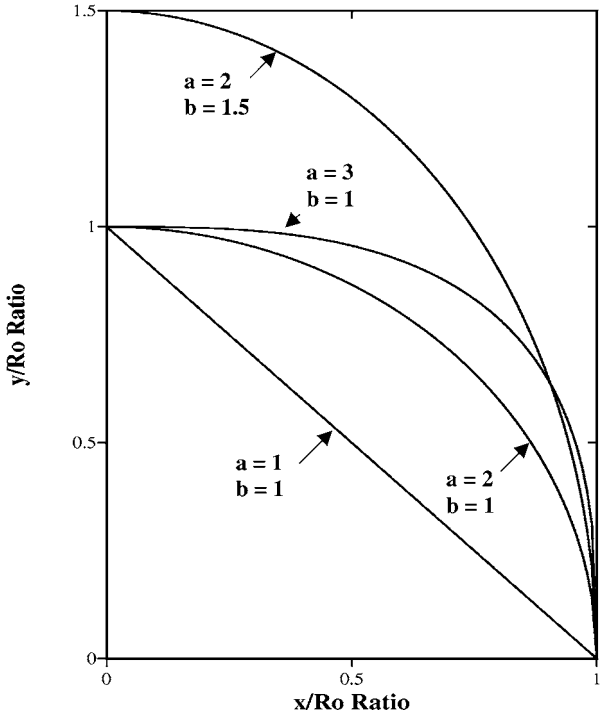

Figure 5 Effect of the two blank-shape design parameters, a and b, on the blank shape in the first quadrant of the x-y plane.

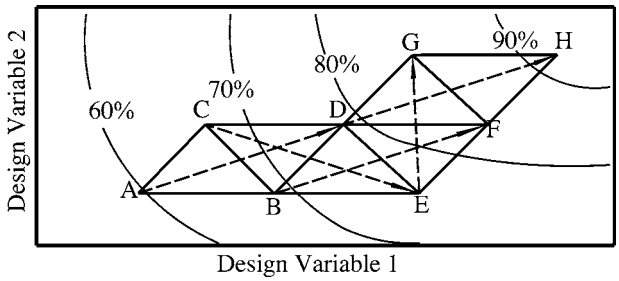

Figure 6 A schematic of the basic Simplex algorithm used for optimization of the blank shape. The initial simplex is represented by the triangle ABC. Dashed lines with an arrow indicate replacement of the prior worst design with a new design by projecting through the centroid of the remaining two prior designs.

Optimization of the shape of the OFHC copper sheet blank is done using the basic Simplex search method [31]. The basic Simplex search method requires that the number of initial evaluations of the objective function (referred to as designs in the following) be one greater than the number of design variables. Since there are two blank-shape design variables, a and b in Equation 37, the simplex method entails that the objective function be initially evaluated for three pairs of design variables. In the $a - b$ two-dimensional search space, the three initial pairs of design variables form a triangle (A – B – C), Fig. 6, which is generally referred to as the initial simplex. The three initial designs are ranked according to the magnitude of the objective function. The design with the largest value of the objective function (design A in Fig. 6) is ranked as worst. The optimum design (the design associated with a minimum value of the objective function) corresponds to a 100% point in Fig. 6. Next, design A is reflected through the centroid of the other two designs to obtain a new design, design D in Fig. 6. The new design replaces the prior worst design and a new simplex B – C – D is formed. Designs within the new simplex are ranked again, the worst design, design C, identified, and the aforementioned procedure repeated. To prevent the method from bouncing back and forth between two designs in cases when the new design is the worst design within the new simplex, the simplex algorithm selects the second worst design and reflects it in such cases.

The main advantage of the Simplex method is that it requires evaluation of the objective function but not evaluation of its derivatives. After the initial simplex is formed, one evaluation of the objective function per search step is needed which makes the algorithm very efficient. In addition, the algorithm is very simple and can be easily coupled with a commercial finite element program such as ABAQUS/Explicit. The main limitation of the simplex method is that it, like many other optimization algorithms, may stall at a local minimum. To overcome this limitation, the simplex method must be repeated with several different initial simplexes and the resulting minima ranked. Another potential limitation of the method is that it may require rescaling of the of the design variables to make them all of the same order of magnitude, since all variables are subjected to the same reflection distance. In the present case, the two design variables are comparable to each other since a is expected to be near 2.0 and b near 1.0. Further limitation of the basic Simplex method is that the search progress can be slow. This limitation has been addressed by Nelder and Mead [32] who introduced several modifications which enable expansion or contraction of the simplex in a direction in which the optimization conditions are favorable. These modifications are, however, practical only when the number of design variables is large and when evaluation of the objective function is not time consuming. Since in the present work, there are only two design variables and the evaluation of the objective function involves a finite element simulation by ABAQUS/Explicit and post processing of the results, which are quite time consuming, the basic Simplex search method is used.

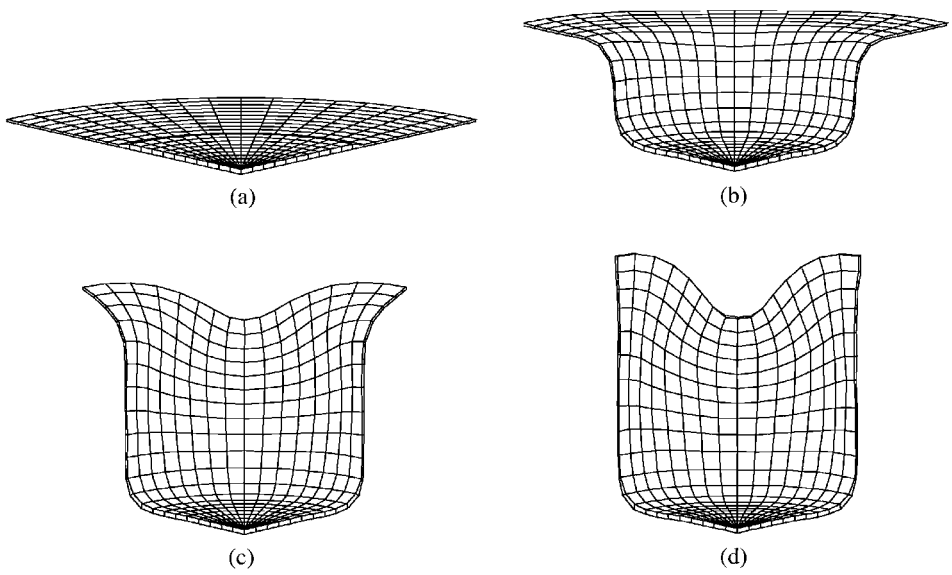

Figure 7 The initial mesh (a) and a sequence of three deformed meshes (b)-(d) generated at equal time intervals during deep drawing of a cylindrical cup from a circular blank (blank-shape parameters $a = 2.0$, $b = 1.0$). To denote the portion of the original blank subject to the clamping force, a 50% reduction factor is applied when showing the corresponding blank thickness.

4. Results and discussion

The initial mesh and a sequence of three deformed meshes obtained at equal time intervals during the simulation of deep drawing of a cylindrical cup from a circular blank, (i.e. from a blank with the shape parameters $a = 2.0$, $b = 1.0$) are shown in Fig. 7a–d. To show the effect of force applied to the blankholder, the resulting reduction in blank thickness is displayed in Fig. 7a with a magnification factor 10. The number and the location of rim ears along the rolling and the transverse direction and rim trough along a direction nearly halfway between the rolling and the transverse directions, Fig. 7d is in general agreement with the experimentally measured earing in polycrystalline aluminum [e.g. 4], a material with the same (f.c.c.) crystal structure. Fig. 7d shows that earing is highly pronounced in the fully-drawn cup. In the manufacturing practice, this would not only entail trimming as an additional operation but would also create considerable amount of scrap, which must be handled and recovered.

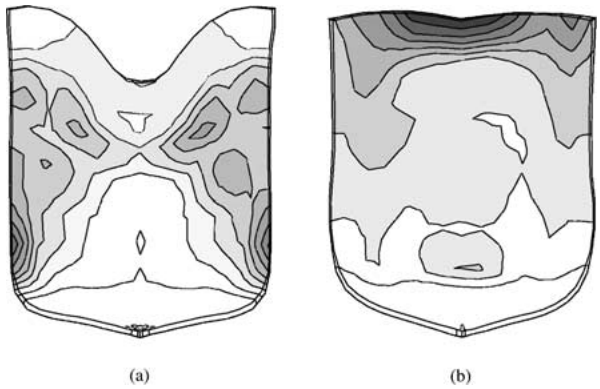

Figure 8 Distribution of the equivalent plastic strain in a cylindrical cup drawn from: (a) a circular blank and: (b) a blank with the shape parameters $a = 4.0$, $b = 1.0$. The highest strain levels are denoted by the darkest shade of gray. The strain ranges are: (a) 0.07–2.0 and; (b) 0.06–2.7.

Fig. 8a shows the distribution of equivalent plastic strain in the cylindrical cup drawn from a circular blank. The equivalent plastic strain ranges between 0.06 (denoted by the lightest shade of gray) and 2.7 (denoted by the darkest shade of gray). The highest level of equivalent plastic strain is observed in the radial directions in which cup ears form. A careful examination of Figs 8a and 7d shows that in the high equivalent strain regions the cup wall has undergone a considerable reduction in thickness. This would usually cause cracking of the cup wall.

Based on the cup height profile and the location of cup ears shown in Fig. 7d, it was decided to reduce the blank radius to 47.8 mm and to form the initial simplex using the following three pairs of values for the blank-shape parameters, a and b: (4.0,1.0), (4.0,1.05), (4.25,1.0). Fig. 9a–d show the initial mesh and a sequence of three deformed meshes obtained at equal time intervals during the simulation of cup drawing from a blank with the shape parameters $a = 4.0$, $b = 1.0$. The extent of earing in the fully-drawn cup in this case, Fig. 9d, is significantly lower than that in the cup drawn from a circular blank, Fig. 7d.

Fig. 8b shows the distribution of equivalent plastic strain in the cylindrical cup drawn from a blank characterized by the shape-parameters $a = 4.0$, $b = 1.0$. The equivalent plastic strain ranges between 0.07 (denoted by the lightest shade of gray) to 2.0 (denoted by the darkest shade of gray). This is a slightly narrower range than that shown in Fig. 8a. The highest level of the equivalent plastic strain is observed near the cup rim in the radial directions in which the trough forms. A comparison of Figs 8b and 9d with Figs 8a and 7d shows that the wall thickness is significantly more uniform in the cup drawn from a blank characterized by the shape parameters, $a = 4.0$, $b = 1.0$ then in the cup drawn from a circular blank.

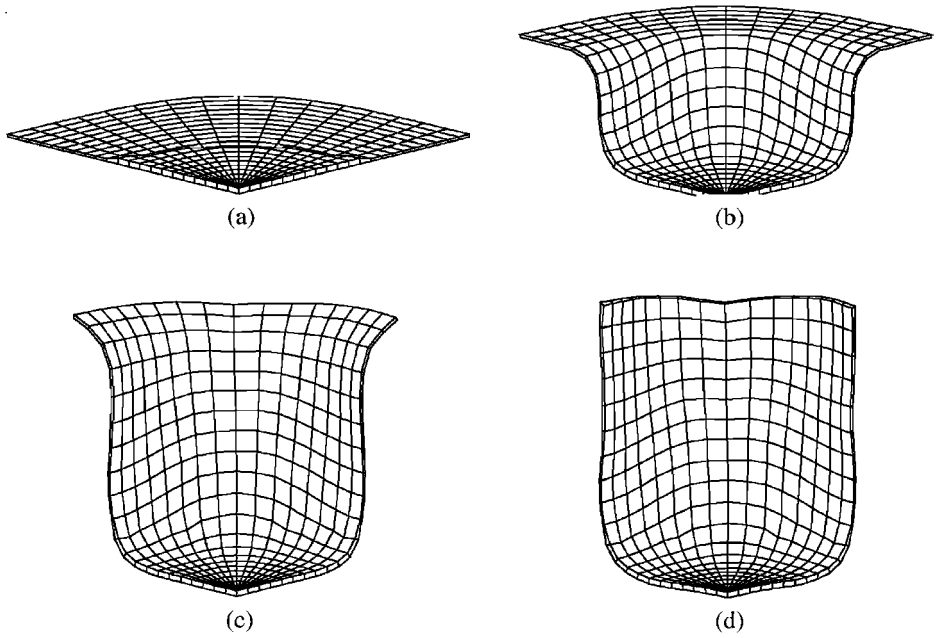

Figure 9 The initial mesh (a) and a sequence of three deformed meshes (b)–(d) generated at equal time intervals during deep drawing of a cylindrical cup from a blank whose shape is characterized by the shape parameters $a = 4.0$, $b = 1.0$.

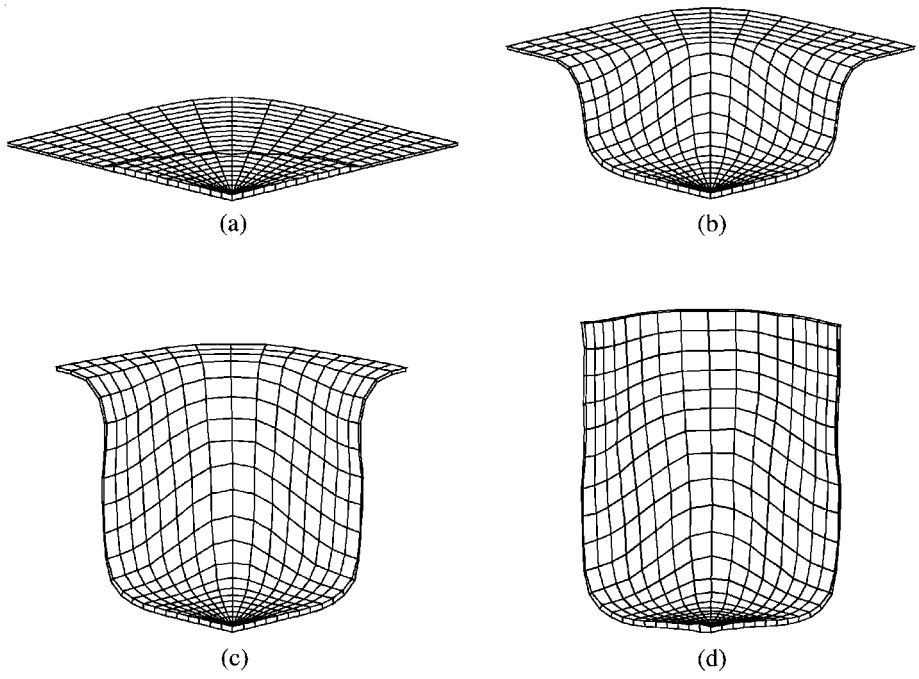

Figure 10 The initial mesh (a) and a sequence of three deformed meshes (b)–(d) generated at equal time intervals during deep drawing of a cylindrical cup from a blank with the optimum shape, i.e. the shape characterized by the shape parameters $a = 5.5$, $b = 1.05$.

Fig. 10a–d show the initial mesh and a sequence of three deformed meshes obtained during the simulation of deep drawing of a cylindrical cup from a blank with the optimum shape, i.e., the shape corresponding to the parameters $a = 5.5$ and $b = 1.05$. It is evident that earing has been almost entirely eliminated and that the height of the fully-drawn cup appears quite uniform around its rim. Further improvements in the uniformity of the cup height could be achieved by continuing the optimization procedure with a smaller size of the initial simplex.

Fig. 11 shows the variation of the cup height along its rim upon the completion of the deep drawing process for three values of the blank-shape parameters, a and b. The variation of the cup height for the circular shape of the blank is indicated as $a = 2.0$, $b = 1.0$. The optimum blank shape obtained after ten optimization steps following formation of the initial simplex are denoted as $a = 5.5$ and $b = 1.05$.

The extent of earing in fully-drawn cups can be quantified using the magnitude of the objective function, G, Equation 38. Fig. 12 shows the progress of reduction of the extent of earing during optimization of the blank shape. The extent of earing in the cup drawn from a circular blank is denoted by the step number -3, while step numbers -2, -1 and 0 are used to denote the initial simplex. The results shown in Fig. 12 show that the extent of earing continues to decrease as optimization proceeds (optimization step numbers zero and higher). The optimum blank shape, characterized by the shape-parameters $a = 5.5$ and $b = 1.05$, is obtained after ten optimization steps past the stage of formation of the initial simplex. The optimization procedure is terminated when the absolute value of the change in the objective function divided by the magnitude of the objective function fell below 0.01. It should be noted that the extent of earing in the cup drawn from a blank with the optimum shape is only 1.35% of the extent of earing in the cup drawn from a circular blank.

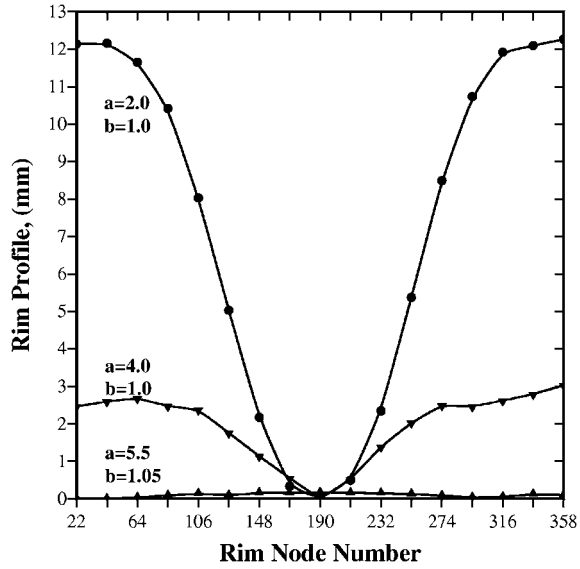

Figure 11 Variation of the cup height along its rim for various initial shapes of the blank. The circular blank is denoted as $a = 2$, $b = 1$ and the blank with the optimized shape as $a = 5.5$, $b = 1.05$.

In summary, the results of the blank-shape optimization indicate that, as one would expect, in order to minimize the extent of earing in fully-drawn cylindrical cups, the blank shape should be changed from the circular one in such a way that more material is added in the radial direction in which troughs form. It should be also noted that in addition to minimizing the extent of earing, uniformity in the cup-wall thickness, cup-roundness, the uniformity in its radius etc., are also important issues which must be addressed in the attempt

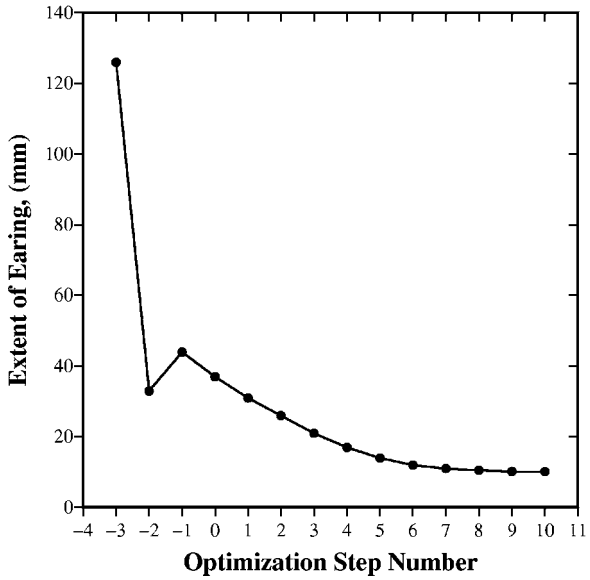

Figure 12 The progress of reduction of the extent of earing during the blank-shape optimization process.

to improve the quality of the as-drawn product. Some of these multi-objective optimization problems are being addressed in our current work [33].

5. Conclusions

Based on the results obtained in the present work the following conclusions can be made:

(1) Earing along the rim of full-drawn cylindrical OFHC-copper cups resulting from the as-rolled crystallographic texture in this material can be predicted by carrying out finite element simulations of the deep-drawing process.

(2) To account for the effects of crystallographic texture present in the blank material, one may use crystal-plasticity type materials constitutive relations which assign crystallographic orientation to each grain and enable the prediction of reorientation of the grains during deformation.

(3) By proper selection of the blank shape, the extent of rim earing can be reduced to the point that its trimming from the fully-drawn cups may not be required. Should trimming be required to permit the cup ends to be attached properly, scrap will be minimal and hence its handling and recovery will not be a major problem.

Acknowledgements

The material presented here is based on work supported by the National Science Foundation, Grant Numbers DMR-9906268 and CMS-9531930 and by the U.S. Army Grant Number DAAH04-96-1-0197. The authors are indebted to Drs. Bruce A. MacDonald and K.J. Murty of NSF and Dr. David Stepp of ARO for the continuing interest in the present work. A constructive discussion held with Professor Georges Fadel is greatly appreciated. The authors also acknowledge the support of the Office of High Performance Computing Facilities at Clemson University.

References

1. G. E. G. TUCKER, *Acta Metall.* **9** (1961) 275.
2. D. V. WILSON and R. D. BUTLER, *Journal of the Institute of Metals* **90** (1961) 473.
3. R. BECKER, R. E. SMELSER and S. PANCHANADEESWARAN, *Modeling and Simulations in Material Science and Engineering* **1** (1993) 203.
4. L. ANAND and S. BALASUBRAMANIAN, *J. Appl. Mech.* **33** (1998) 100.
5. M. GRUJICIC, Unpublished work.
6. C. A. TEODOSIU, in Proceedings of the Conference on Fundamental Aspects of Dislocation Theory, 1970, edited by R. Simmons, J. A. de Wit and R. Bullough, p. 837.
7. R. HILL and J. R. RICE, *Journal of the Mechanics and Physics of Solids* **20** (1972) 401.
8. J. MANDEL, in Proceedings of the International Symposium on Foundations of Continuum Thermodynamics, edited by D. Domingos, J. J. Nina, J. H. Whitlaw (McMillan, London, 1974) p. 283.
9. C. TEODOSIU and F. SIDOROFF, *International Journal of Engineering Science* **14** (1976) 165.
10. R. J. ASARO and J. R. RICE, *Journal of the Mechanics and Physics of Solids* **25** (1977) 309.
11. R. J. ASARO, *Advances in Applied Mechanics* **23** (1983) p. 1; *ASME Journal of Applied Mechanics* **50** (1983) 921.
12. H. CONRAD, *Journal of Metals* **16** (1964) 582.
13. U. F. KOCKS, A. S. ARGON and M. F. ASHBY, in "Progress in Material Science" (Pergamon Press, London, 1975).
14. H. J. FROST and M. F. ASHBY, "Deformation Mechanism Maps" (Pergamon Press, New York, 1982).
15. A. S. ARGON, in "Physical Metallurgy" edited by R. W. Cahn and P. Haasen (Elsevier, Amsterdam, 1995).
16. E. OROWAN, *Phil. Trans. R. Soc. London A* **52** (1940) 8.
17. A. S. ARGON and G. H. EAST, in Proceedings of the 5th International Conference on the Strength of Metals and Alloys, edited by P. Haasen, V. Gerold and G. Kostorz (Pergamon Press, Oxford, 1979) p. 9.
18. A. H. COTRELL and R. J. STOKES, *Proceedings of the Royal Society of London A* **233** (1955) 17.
19. D. PEIRCE, R. J. ASARO and A. NEEDLEMAN, *Acta Metall.* **30** (1982) 1087.
20. R. J. ASARO and A. NEEDLEMAN, *Acta Metall.* **33** (1985) 923.
21. K. S. HAVNER, "Finite Plastic Deformation of Crystalline Solids," 1st ed. (Cambridge University Press, Cambridge, UK, 1992).
22. J. L. BASSANI, *Advances in Applied Mechanics* **30** (1993) 191.
23. S. R. KALIDINDI, C. A. BRONKHORST and L. ANAND, *Journal of the Mechanics and Physics of Solids* **40** (1992) 536.
24. G. I. TAYLOR, in "Stephen Timoshenko 60th Anniversary Volume" (McMillan, New York, 1938) p. 218.
25. *Idem.*, *Journal of the Institute of Metals* **62** (1938) 307.
26. C. A. BRONKHORST, S. R. KALIDINDI and L. ANAND, *Phil. Trans. R. Soc. London A* **341** (1992) 443.
27. M. KOTHARI and L. ANAND, *Journal of the Mechanics and Physics of Solids* (1997).
28. ABAQUS/Explicit 5.8. Hibbit, Karlsson & Sorenson, Inc., Providence, R. I. *ABAQUS Reference Manuals, 1998*.
29. J. C. NAGTEGAAL and L. M. TAYLOR, **242** (1968) 1317.
30. A. M. LUSH, Ph.D thesis, Massachusetts Institute of Technology, June 1990.
31. WALTERS, PARKER, MORGAN and DEMING (eds)., "Sequential Simplex Optimization. A Technique for Improving Quality and Productivity in Research, Development, and Manufacturing" (CRC Press, Boca Raton, FL, 1991).
32. J. A. NELDER and R. A. MEAD, *Computer Journal* **7** (1965) 308.
33. M. GRUJICIC, in prepration.

Received 18 January
and accepted 2 October 2001